Effect of filler shape, volume fraction and loading rate on dynamic fracture behavior of glass-filled epoxy

CrossMark

Vinod Kushvaha, Hareesh Tippur *

Department of Mechanical Engineering, Auburn University, AL 36849, United States

ABSTRACT

The effect of filler shape and filler volume fraction on the dynamic fracture behavior of particulate polymer composites (PPC) has been studied. Mode-I dynamic fracture experiments were carried out on pre-notched glass-filled epoxy. An experimental setup comprising of a gas-gun and a long-bar was used to deliver one-point impact loading to unconstrained specimens. Pulse shapers were utilized to control the loading rate during impact loading. The dynamic crack initiation and propagation events were captured using high-speed photography ($\sim$300,000 frames per second). Digital Image Correlation (DIC) method was utilized to measure in-plane displacement fields around the crack-tip and extract fracture parameters including stress intensity factor histories to examine the filler shape, volume fraction and loading rate effects. The results showed a pronounced improvement in crack initiation toughness for rod-shaped fillers producing $\sim$145% increase over unfilled epoxy at 15% V_f with flakes and spherical fillers showing $\sim$97% and $\sim$67% improvement, respectively. For all three different volume fractions – 5%, 10%, and 15% – considered, the rod-shaped fillers produced the highest crack initiation toughness as well as post-initiation stress intensity factors followed by flakes and spheres, respectively. A linear relationship between crack initiation toughness and log of filler aspect ratio was also recorded. In addition, for 10% V_f rod-shaped filler case, the effect of loading rate on dynamic fracture behavior has been examined. The loading rate study showed $\sim$113% and $\sim$50% increase in crack initiation toughness for the lowest and the highest loading rate cases, respectively, compared to that of neat epoxy.

© 2014 Elsevier Ltd. All rights reserved.

1. Introduction

Particle-filled polymer composites (PPC) have been widely used in various engineering fields due to their excellent mechanical properties, chemical resistance, and electrical insulation. More importantly, they are also relatively easy to process at low costs and the overall properties can be tailored by choosing the filler and/or its volume fraction in the composite. Unlike traditional fiber reinforced composites, simplicity of PPC in terms of macroscopic isotropy is another aspect which often makes them quite desirable for mechanical design. Therefore, understanding the role of filler concentration, filler size and shape, and filler interfacial strength with the polymer matrix on the macromechanical properties such as stiffness, strength and toughness of the resulting PPC is critical.

Polymers are normally modified by adding inorganic-particulate fillers such as alumina, mica or silica, to name a few [1–9]. Song et al. studied the particle shape effects on the fracture and ductility of spherical and an irregularly shaped particle-reinforced Al-6061 composite containing 20% Al_2O_3 by volume under quasi-static tensile loading [10]. The spherical particles produced a slightly lower yield strength and work hardening rate but considerably higher ductility than the irregular particle counterpart. Their finite element analysis results indicate that the distinction between the failure modes for these two composites can be attributed to the differences in the development of internal stresses and strains within the composite due to particle shape. Nakamura et al. examined the effect of particle size on the static fracture behavior of epoxy filled with different size (ranging from 6 to 42 μm) spherical silica particles [11]. They observed increase in both energy release rate and fracture toughness with particle size. Fractography showed a relatively smooth fracture surface with small particles (6 μm) and a rough surface with large particles (caused by crack deflections around large particles). Wu analytically studied the effect of inclusion shape on the elastic modulus of two phase solids [12]. Their disk-shaped inclusions showed the maximum enhancement in elastic modulus compared to needles and spheres. The effect of particle size (4.5–62 μm) on the elastic modulus of epoxy/spherical glass particle composites were examined by

* Corresponding author. Tel.: +1 334 844 3327.
  E-mail address: tippuhv@auburn.edu (H. Tippur).

Spanoudakis et al. [13]. At lower volume fractions (V_f) (10–18%), the modulus was nearly independent of particle size. For higher V_f (30–46%), there was a slight decrease in modulus with increasing particle size. In a similar study, the effect of particle size on the modulus of epoxy/spherical and irregularly-shaped silica composites have been explored [14] for a size range of 2–30 μm and the modulus was observed to remain constant with particle size. Kitey and Tippur studied the role of particle size in the dynamic fracture behavior of glass-filled epoxy using optical interferrometry and high-speed photography [15]. Spherical particles (ranging from 7 to 200 μm) were used in their work to reinforce epoxy at a constant 10% V_f. The elastic characteristics were unaffected by the filler size, whereas fracture toughness increased with size from 7 to 35 μm and then decreased from 35 to 200 μm.

The existing literature in this area suggests that the particle shape effect on fracture toughness for particulate composites is largely unexplored. Therefore, the focus of the present study is to understand the effect of filler shape and their volume fraction on fracture behavior of glass-filled epoxy composites, particularly under *dynamic* loading conditions. However, the failure of the PPC could initiate differently under different loading rates [2,16–21]. Hence, to bridge this gap, the loading rate effects, characterized by the rate of change of stress intensity factor, on dynamic fracture behavior of epoxy filled with 10% V_f rod-shaped filler were also studied since this filler shape produced a large improvement in fracture toughness.

2. Material preparation

Glass fillers of similar density and size scale, but differing aspect ratios (flakes, rods, and spheres; see Table 1) were chosen to study their relative shape effects on the dynamic fracture mechanisms of PPC (Fig 1). None of the fillers used had their surface modified by wetting agents and this was guided by the earlier work by Kitey and Tippur [22] showing uncoated fillers produce better fracture characteristics under dynamic loading conditions.

The glass fillers were dispersed into a low-viscosity epoxy (Epo-Thin, from Beuhler Inc., USA; Bisphenol-A resin and Amine based hardener; densities 1130 kg/m^3 and 961 kg/m^3, respectively). To carry out the dynamic fracture study, glass-filled epoxy (containing 0% (neat epoxy), 5%, 10% and 15% glass filler by volume, respectively) sheets were cast. To ensure uniform dispersion, fillers were added into the epoxy resin and stirred using a stirrer and then degassed until the mixture appeared to be free from trapped air bubbles. Subsequently, stoichiometric proportion of hardener was added to the mixture and stirred until it gelled to avoid settlement of filler particles before pouring into the mold. Upon curing for a minimum of 7 days, the sheets were demolded and machined into rectangular specimens of dimensions 60 mm × 30 mm × 9 mm (Fig. 2(a)). An edge notch of 6 mm length was introduced at the mid-span of each specimen using a diamond impregnated circular saw and the notch tip was sharpened using a sharp razor blade. The uniformity of filler dispersion was confirmed subsequently using SEM images of fractured specimen surfaces. Fractographs at four different locations for 15% V_f rod-shaped glass-filled epoxy are shown in Fig. 2(b). The 15% V_f rod-shaped filler example is

presented here as they tend to be most prone to agglomeration. However, as evident from the micrographs, agglomerations are largely absent.

3. Physical and elastic properties

Physical and elastic properties were measured for all PPC and are tabulated in Table 2. Ultrasonic transducers (for longitudinal wave: Panametrics #V129 RM, 10 MHz; for shear wave: Panametrics #V156 RM, 5 MHz) coupled with a signal analyzer and an oscilloscope were used to perform pulse-echo measurements to determine the longitudinal (C_l) and shear wave (C_s) speeds at discrete locations of the cast sheet. After measuring the material density (ρ), dynamic elastic modulus (E_d) and Poisson's ratio (υ_d) were calculated from expression for C_l and C_s, $C_l = \sqrt{\frac{E_d(1-\nu_d)}{\rho(1+\nu_d)(1-2\nu_d)}}$, $C_s = \sqrt{\frac{E_d}{2\rho(1+\nu_d)}}$. Thus measured physical and elastic properties are shown in Table 2. It should be noted that relative to neat epoxy, ρ, C_l, C_s and E_d of the composites with 5%, 10% and 15% V_f of fillers show a monotonic increase whereas the shape of the filler seems to produce negligible variation at a constant V_f.

4. Experimental details

4.1. Dynamic tests

A schematic of the experimental setup used for dynamic fracture tests is shown in Fig. 3. The setup included a 1.83 m long, 25.4 mm diameter long-bar with a 6.35 mm diameter bull-nose tip registered against an unconstrained specimen and a 304.8 mm long, 25.4 mm diameter striker held inside the barrel of a gas-gun. Both the long-bar and the striker were of the same diameter and made of aluminum 7075-T6. This eliminated the impedance mismatch between the long-bar and the striker. Three different dynamic loading rates were achieved by using different pulse shapers between the striker and the long-bar shown in Fig. 3 [23]. A soft Aluminum 1100 disc (hereon designated as 'Al-PS') of diameter 8 mm and thickness 0.9 mm produced a *strain-rate* of 10.7/s, *measured on the long-bar* by a strain gage during impact. A combined polycarbonate washer (outer diameter 6.3 mm, inner diameter 2.2 mm and thickness 0.7 mm) and Al 1100 disc sandwich pulse shaper (hereon designated as 'PC-PS') produced a lower strain rate of 3.7/s relative to Al-PS. The highest strain rate of 42.0/s was attained when no pulse shaper (hereon designated as 'No-PS') was used. The role of the pulse shaper was to ramp up the stress wave in a controlled fashion in the long-bar during impact [24]. The striker was launched towards the long-bar using the gas-gun at a velocity of ~16 m/s. When the striker contacted the long-bar, a compressive stress wave was initiated and propagated through the bar before transmission into the specimen.

A stochastic black and white speckle pattern was sprayed on to the specimen surface for performing in-plane deformation measurement using 2D DIC method. The pattern was photographed using a Cordin-550 ultrahigh-speed digital camera (Cordin Scientific Imaging, Salt Lake City, UT, USA) equipped with 32 independent CCD image sensors (1000 × 1000 pixels) positioned

Table 1
Glass Filler Characteristics.

Shape	Source	Average dimensions	Aspect ratio[*](AR)	Density (kg/m^3)
Flake	ACF-300: Isorca Inc., USA	30 μm wide, 5 μm thick	30/5 = 6	2,500
Rod	Milled Fiber: Fiberglass Supply, USA	800 μm long, 10 μm diameter	800/10 = 80	2,500
Sphere	A300: Potters Industries, USA	35 μm diameter	35/35 = 1	2,500

[*] Aspect Ratio was determined by dividing the largest average dimension by the shortest average for each filler type, provided by the manufacturer.
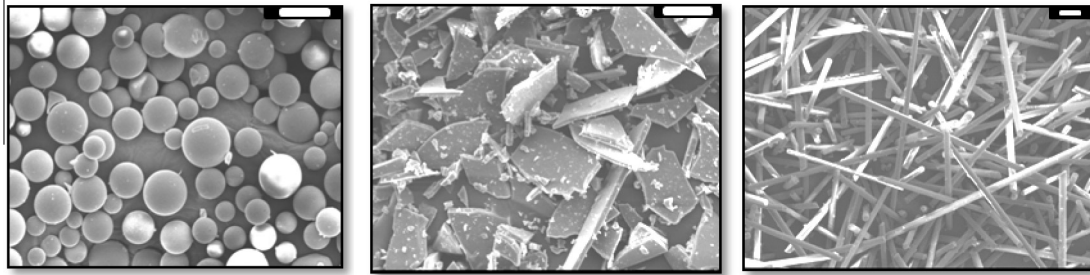
Fig. 1. SEM micrographs of sphere-, flake- and rod-shaped glass fillers used in present study (left to right respectively; scale bar: 50 μm).
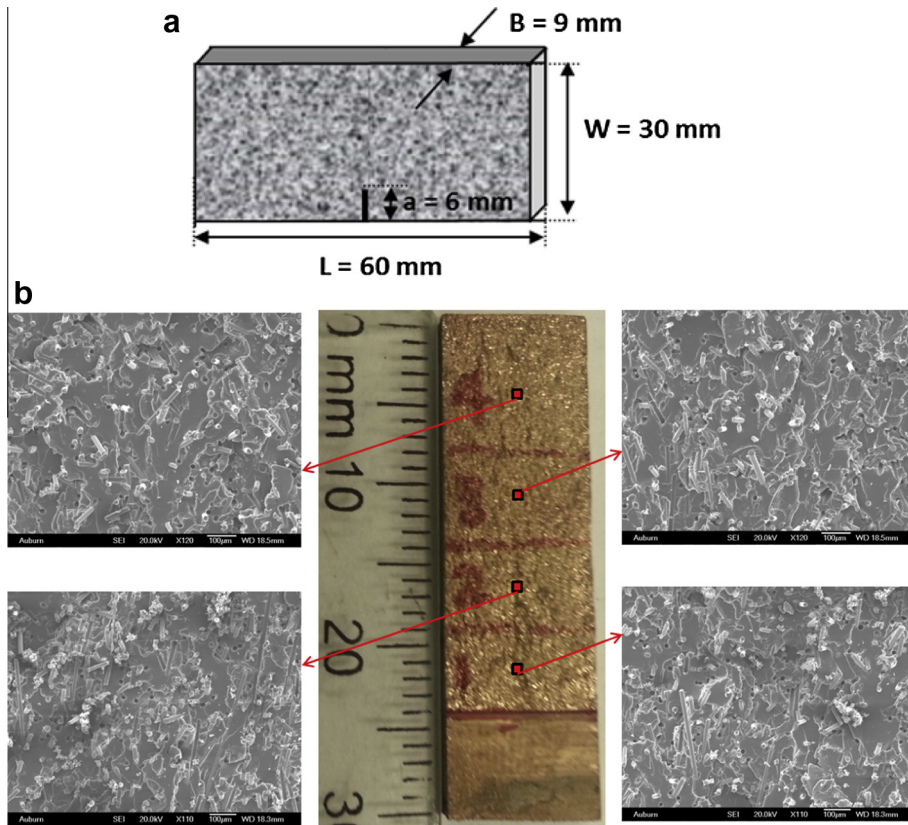

Fig. 2. (a) Schematic of test specimen, (b) typical fractogrpahs at four different locations for 15% V_f rod-shaped glass-filled epoxy (micrograph scale bar = 100 μm); Note the uniformity of filler dispersion.

Table 2
Material properties of glass-filled epoxy composite.

Particle type	Density ρ (kg/m³)	Longitudinal wave speed C_l (m/s)	Shear wave speed C_s (m/s)	Elastic modulus E_d (GPa)	Poisson's ratio v_d
(a) V_f = 5%					
Epoxy	1146 ± 10	2481 ± 12	1128 ± 3	3.99	0.37
Sphere	1222 ± 12	2534 ± 8	1177 ± 3	4.62	0.36
Flake	1225 ± 11	2526 ± 6	1187 ± 6	4.69	0.36
Rod	1226 ± 12	2534 ± 22	1188 ± 7	4.68	0.36
(b) V_f = 10%					
Sphere	1286 ± 9	2553 ± 6	1207 ± 4	5.08	0.36
Flake	1288 ± 8	2571 ± 9	1248 ± 11	5.40	0.35
Rod	1285 ± 11	2534 ± 6	1243 ± 7	5.33	0.34
(c) V_f = 15%					
Sphere	1358 ± 9	2600 ± 6	1243 ± 5	5.67	0.35
Flake	1361 ± 7	2630 ± 6	1300 ± 6	6.16	0.34
Rod	1375 ± 8	2598 ± 12	1286 ± 9	6.08	0.34

circumferentially around a rotating mirror which sweeps light over the sensors. Prior to loading, a set of 32 images corresponding to the undeformed state of the specimen were recorded at a rate of ~300,000 frames per second. To record a second set of 32 images corresponding to the deformed state of the specimen, the striker was launched towards the long-bar by discharging the gas-gun.
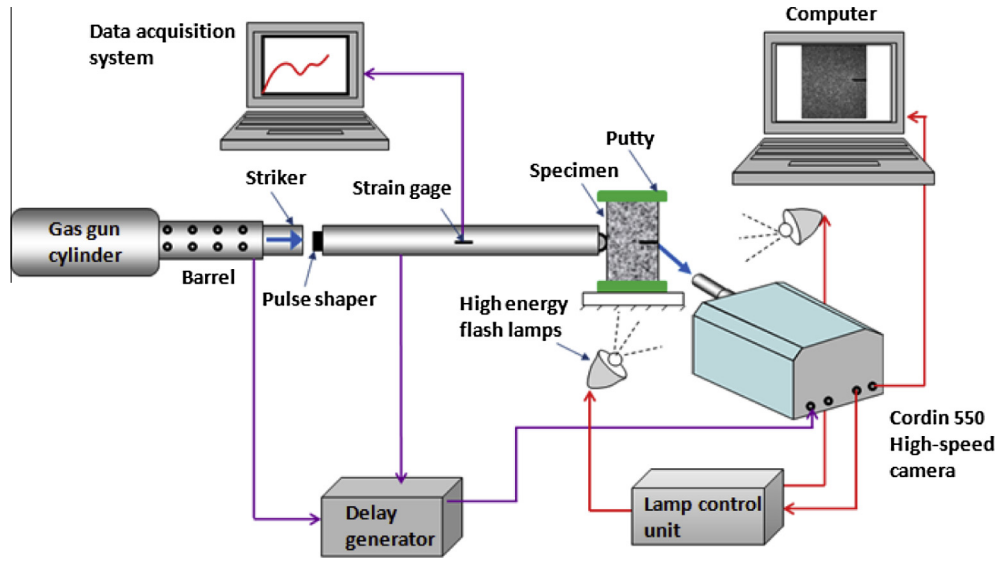
Fig. 3. Schematic of experimental setup.

When the striker contacted the long-bar, it completed an electrical circuit, signaling a delay generator to trigger the camera. The camera in turn triggered a pair of high energy flash lamps and initiated image capture at the same framing rate. Thus, each image in the undeformed (reference) set had a corresponding image in the deformed set. The recorded sets of deformed and undeformed images were then correlated to obtain in-plane displacement components.

5. Optical data analysis

The recorded undeformed and deformed sets of images were correlated using a digital image correlation tool ARAMIS™ (GOM mbH, Germany) and the in-plane crack-opening (u_y) and crack-sliding (u_x) displacement fields were estimated near the crack-tip vicinity. Knowing the asymptotic expressions for a dynamically loaded stationary crack,

$$u_x = \sum_{n=1}^{N} \frac{(K_I)_n}{2\mu}$$
$$\times \frac{r^{n/2}}{\sqrt{2\pi}} \left\{ \kappa \cos \frac{n}{2}\theta - \frac{n}{2} \cos \left(\frac{n}{2}-2\right)\theta + \left\{\frac{n}{2}+(-1)^n\right\} \cos \frac{n}{2}\theta \right\}$$
$$+ \sum_{n=1}^{N} \frac{(K_{II})_n}{2\mu}$$
$$\times \frac{r^{n/2}}{\sqrt{2\pi}} \left\{ \kappa \sin \frac{n}{2}\theta - \frac{n}{2} \sin \left(\frac{n}{2}-2\right)\theta + \left\{\frac{n}{2}-(-1)^n\right\} \sin \frac{n}{2}\theta \right\}$$
$$+ Pr \cos\theta + Qr \sin\theta + u_{0x} \qquad (1)$$

$$u_y = \sum_{n=1}^{N} \frac{(K_I)_n}{2\mu}$$
$$\times \frac{r^{n/2}}{\sqrt{2\pi}} \left\{ \kappa \sin \frac{n}{2}\theta + \frac{n}{2} \sin \left(\frac{n}{2}-2\right)\theta - \left\{\frac{n}{2}+(-1)^n\right\} \sin \frac{n}{2}\theta \right\}$$
$$+ \sum_{n=1}^{N} \frac{(K_{II})_n}{2\mu}$$
$$\times \frac{r^{n/2}}{\sqrt{2\pi}} \left\{ -\kappa \cos \frac{n}{2}\theta - \frac{n}{2} \cos \left(\frac{n}{2}-2\right)\theta + \left\{\frac{n}{2}-(-1)^n\right\} \cos \frac{n}{2}\theta \right\}$$
$$+ Pr \cos\theta + Qr \sin\theta + u_{0y} \qquad (2)$$

where, u_x and u_y represent crack sliding and opening displacements, (r, θ) are crack-tip polar coordinates, κ is $(3 - v)/(1 + v)$ for plane stress where μ and v are shear modulus and Poisson's ratio, respectively; P and Q account for any rigid body rotation [25], and u_{ox} and u_{oy} represent rigid body translation along the x- and y-directions, respectively. The coefficients $(K_I)_n$ and $(K_{II})_n$ of the leading terms (when n = 1) are the mode-I and mode-II dynamic stress intensity factors (SIF), respectively.

Once the crack started propagating, the asymptotic expressions for sliding and opening displacements for a steadily growing crack [26] were evaluated using Eqs. (3) and (4),

$$u_x = \sum_{n=1}^{N} \frac{(K_I)_n B_I(C)}{2\mu} \sqrt{\frac{2}{\pi}} (n+1) \left\{ r_1^{n/2} \cos \frac{n}{2}\theta_1 - h(n) r_2^{n/2} \cos \frac{n}{2}\theta_2 \right\}$$
$$+ \sum_{n=1}^{N} \frac{(K_{II})_n B_{II}(C)}{2\mu} \sqrt{\frac{2}{\pi}} (n+1) \left\{ r_1^{n/2} \sin \frac{n}{2}\theta_1 - h(\bar{n}) r_2^{n/2} \sin \frac{n}{2}\theta_2 \right\}$$
$$+ Pr \cos\theta + Qr \sin\theta + u_{0x} \qquad (3)$$

$$u_y = \sum_{n=1}^{N} \frac{(K_I)_n B_I(C)}{2\mu} \sqrt{\frac{2}{\pi}} (n+1) \left\{ -\beta_1 r_1^{n/2} \sin \frac{n}{2}\theta_1 + \frac{h(n)}{\beta_2} r_2^{n/2} \sin \frac{n}{2}\theta_2 \right\}$$
$$+ \sum_{n=1}^{N} \frac{(K_{II})_n B_{II}(C)}{2\mu} \sqrt{\frac{2}{\pi}} (n+1) \left\{ \beta_1 r_1^{n/2} \cos \frac{n}{2}\theta_1 + \frac{h(\bar{n})}{\beta_2} r_2^{n/2} \cos \frac{n}{2}\theta_2 \right\}$$
$$+ Pr \cos\theta + Qr \sin\theta + u_{0y} \qquad (4)$$

where,

$$r_m = \sqrt{X^2 + \beta_m^2 Y^2}, \quad \theta_m = \tan^{-1}\left(\frac{\beta_m Y}{X}\right), m = 1, 2, \beta_1$$
$$= \sqrt{1 - \left(\frac{c}{C_L}\right)^2}, \beta_2 = \sqrt{1 - \left(\frac{c}{C_S}\right)^2}$$

$$C_L = \sqrt{\frac{(\kappa+1)\mu}{(\kappa-1)\rho}}, C_s = \sqrt{\frac{\mu}{\rho}}, \kappa = \frac{3-v}{1+v},$$

$$B_I(C) = \frac{(1+\beta_2^2)}{D}, \quad B_{II}(C) = \frac{2\beta_2}{D}, \quad D = 4\beta_1\beta_2 - (1+\beta_2^2)^2 \qquad (5)$$

$$h(n) = \begin{cases} \frac{2\beta_1\beta_2}{1+\beta_2^2} & \text{for odd } n \\ \frac{1+\beta_2^2}{2} & \text{for even } n \end{cases} \quad \text{and } h(\bar{n}) = h(n+1)$$

Here (r, θ) and (x, y) are the polar and Cartesian coordinates, respectively, c is the instantaneous crack speed, C_L and C_S are the longitudinal and shear wave speeds for the material, and μ and v are shear modulus and Poisson's ratio, respectively; P and Q define rigid body rotation [25], and u_{0x} and u_{0y} represent rigid body translation along the x- and y-directions, respectively as in Eqs. (1) and (2). Again, coefficients $(K_I)_n$ and $(K_{II})_n$ of the leading terms are the mode-I and mode-II dynamics stress intensity factors, respectively.

In order to extract the SIF history from fracture events, (u_y, u_x) displacement fields were digitized by identifying the current crack-tip location and subsequently establishing the Cartesian and polar coordinates at the crack-tip. A number of data points were collected in the vicinity of the current crack-tip over radial and angular extents of $0.5 < r/B < 1.5$ (where B is sample thickness) and $[(-150° < \theta < -90°)$ and $(90° < \theta < 150°)]$ to avoid regions of dominant 3D deformations and far-field effects [27]. At each data point, the two displacement components (u_y, u_x) as well as the location of these points were stored. For time instants before crack initiation, the asymptotic expressions for a dynamically loaded stationary crack were used to extract mode-I and -II stress intensity factors using an over-deterministic least-squares analysis of the data. For time instants after crack initiation, the asymptotic expressions for sliding and opening displacements for a steadily growing crack were used.

For a mode-I problem, the crack-opening displacements (u_y) are rich in mode-I information whereas crack sliding displacements (u_x) are rich in mode-II information. Thus, u_y and u_x were used to extract mode-I and -II stress intensity factors K_I and K_{II}, respectively. The acquired speckle images for glass-filled epoxy with 10% V_f of spheres for the 'Al-PS' pulse-shaper case with crack opening (u_y) and crack sliding (u_x) displacement, respectively, are shown in Fig. 4. The crack-tip is shown using the arrow in each speckle image. The u_y and u_x fields show that contour lines (in 5 μm increments) and magnitude of displacement (in μm shown by color-bars) are nearly symmetric relative to the crack, consistent with mode-I fracture behavior. The u_x-field plot shows a dense set of isolines emerging from the right-hand side of the contour plots due to impact loading on the edge of the specimen ahead of the initial crack-tip.
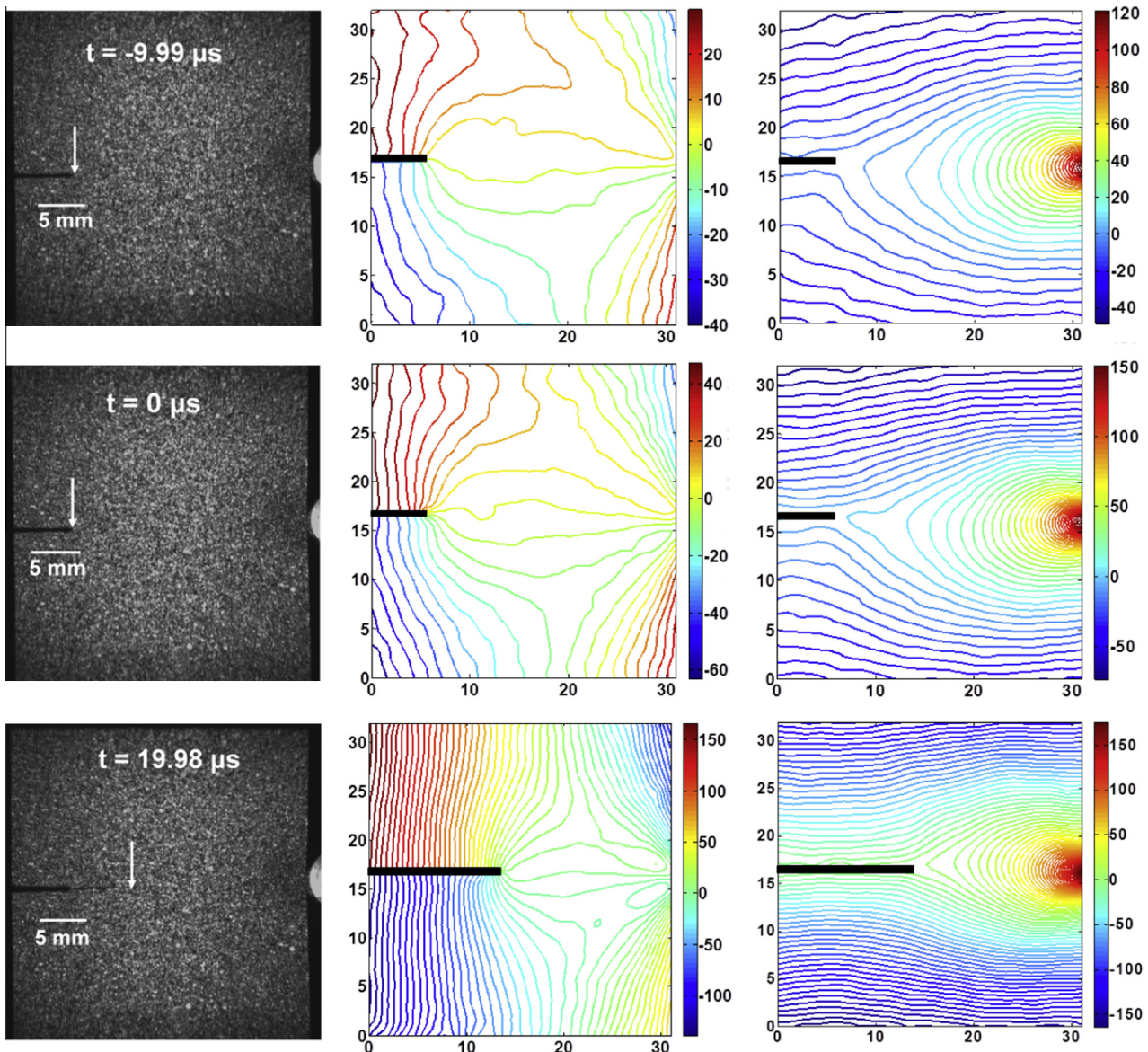

Fig. 4. Acquired speckle images for glass-filled epoxy with 10% V_f of spheres for the 'Al-PS' pulse-shaper case with crack opening (u_y) and crack sliding (u_x) displacement contours in steps of 5 μm, respectively (units on the displacement contour on x- and y-axis are in mm). First row: pre-crack initiation ($t = -9.99$ μs), middle row: crack initiation ($t = 0$ μs), and last row: post-crack initiation ($t = 19.98$ μs) time instants.

6. Experimental repeatability and comparison with finite element simulations

Multiple experiments were conducted for each specimen filled with particles of different shape at different volume fractions (5%, 10% and 15%) to assure experimental repeatability. Fig. 5 shows the SIF histories for two 15% V_f rod-shaped glass-filled epoxy specimens and the 'Al-PS' case. For both specimens, K_I values increases monotonically and nearly overlap on each other up to crack initiation (marked as $t = 0$ μs). The crack initiation is associated with a noticeable drop in the rate of increase of K_I. Subsequent K_I history shows an increasing trend with an oscillatory behavior due to the random distribution of fillers in the crack path as well as a finite specimen size causing stress wave reflections from the free boundaries. The crack being loaded symmetrically, the extracted values of K_{II} histories are negligible within the measurement errors, which further confirms a mode-I event. The mode-II histories can be used here as a guide to estimate errors associated with the SIF extraction method employed.

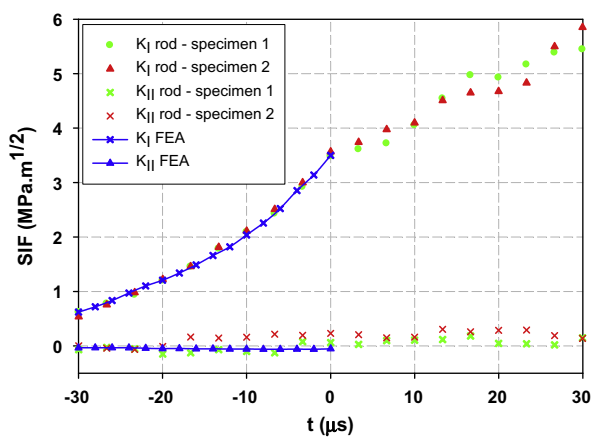The strain history on the long-bar was recorded by a strain gage affixed to it. The strain history for the case of 'Al-PS' pulse shaper is shown in Fig. 6. Subsequently, the particle velocity in the long-bar was calculated [28] using the measured strain history as boundary condition for a companion finite element (FE) simulation. A 3D elasto-dynamic simulation was carried out in ABAQUS/explicit up to crack initiation. Four-node tetrahedron elements were used to simulate 15% glass-filled epoxy specimen with rod-shaped fillers. The long-bar impacting the notched specimen was included in the numerical model. The mesh and material properties used in the FE analysis are shown in Fig. 6. The crack-tip and contact region of the long-bar with the specimen were finely discretized. Both the specimen and long-bar were unconstrained and were butted against each other with a frictionless contact. The cross-sectional area of the long-bar was loaded at the other far-end with particle velocity input recorded during the test. The instantaneous crack-opening and crack-sliding displacements were obtained from the FE simulation. Subsequently, the SIF histories were generated using regression analyses of crack face opening and sliding displacements up to crack initiation [29]. The SIF history obtained from FE analysis shows a good agreement with the experimental results (Fig. 5).

7. Results

7.1. Effect of filler shape

The filler shape effect on the dynamic fracture behavior was studied by comparing the SIF histories for different glass fillers at 5%, 10% and 15% V_f in epoxy for the 'Al-PS' case (Table 3). Plots of K_I histories are shown in Figs. 7(a)–(c) for 5%, 10% and 15% V_f, respectively. The data from both pre- and post-crack initiation periods are included. It should be noted that the measured histories of each sample have been shifted along the time axis to make crack initiation time (identified as $t = 0$) of each experiment coincide. For all volume fractions, the K_I histories show a monotonic increase until and after crack initiation. A modest kink in the history is noticeable in some cases at crack initiation depending on when the crack initiated during the inter-frame period. Among all the three volume fractions, the rod-shaped fillers produced the highest crack initiation toughness as well post-initiation K_I values. The histories for flakes and spheres, respectively, follow successively. Also, for all the three volume fractions, the rate of increase of K_I followed a similar trend up to pre-crack initiation. The rate of increase of K_I was approximately constant for all shapes of fillers, once the crack starts propagating. For 5% V_f (Fig. 7(a)), rod,
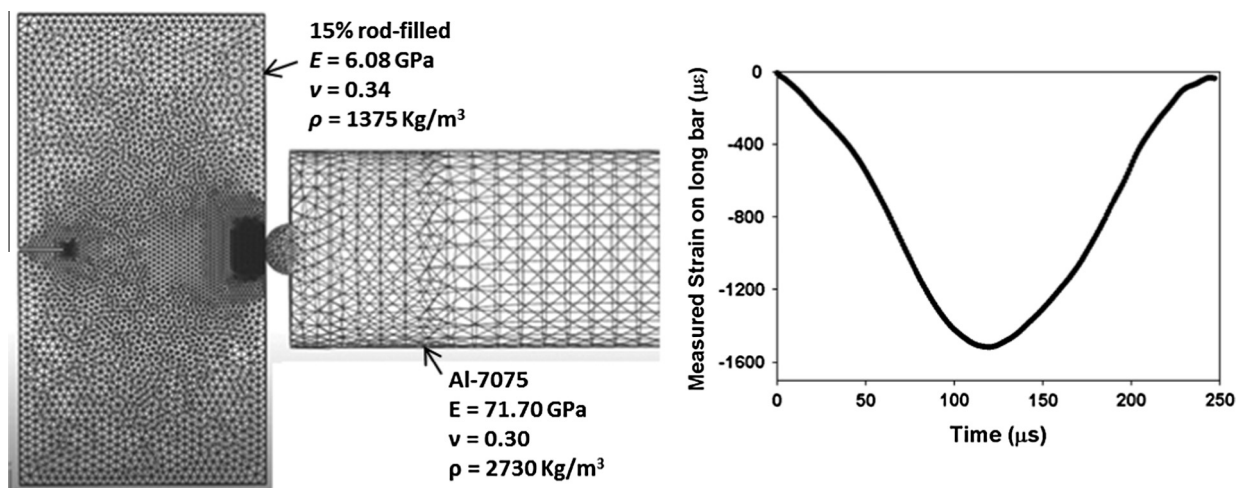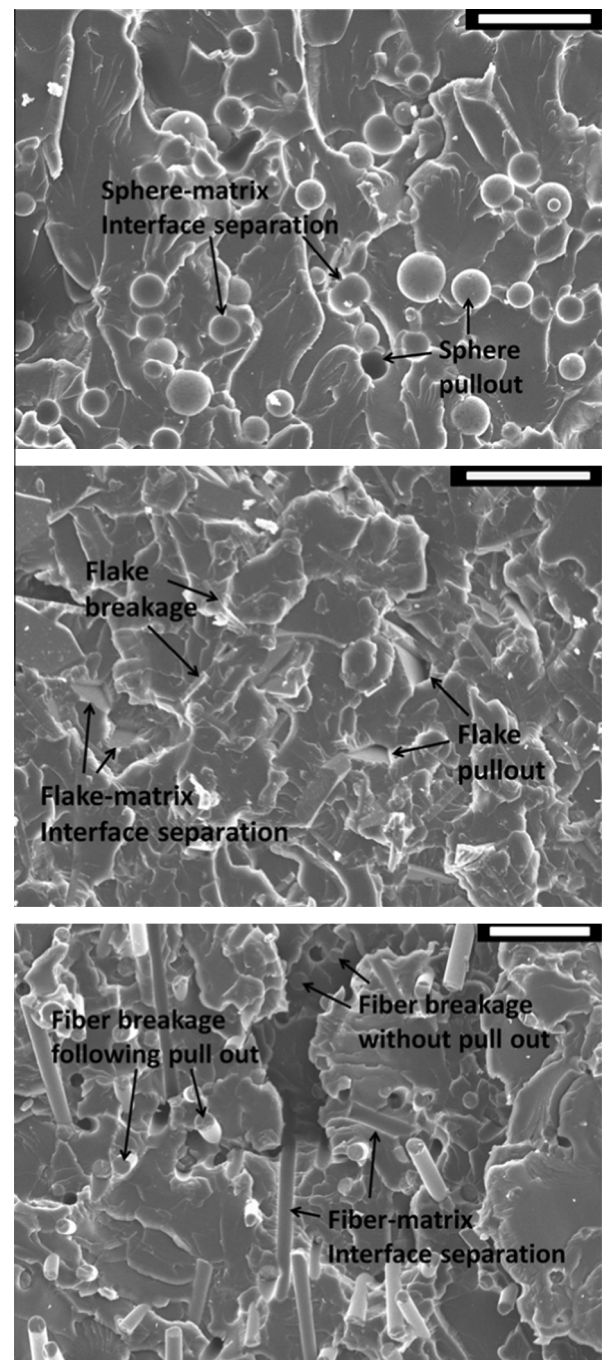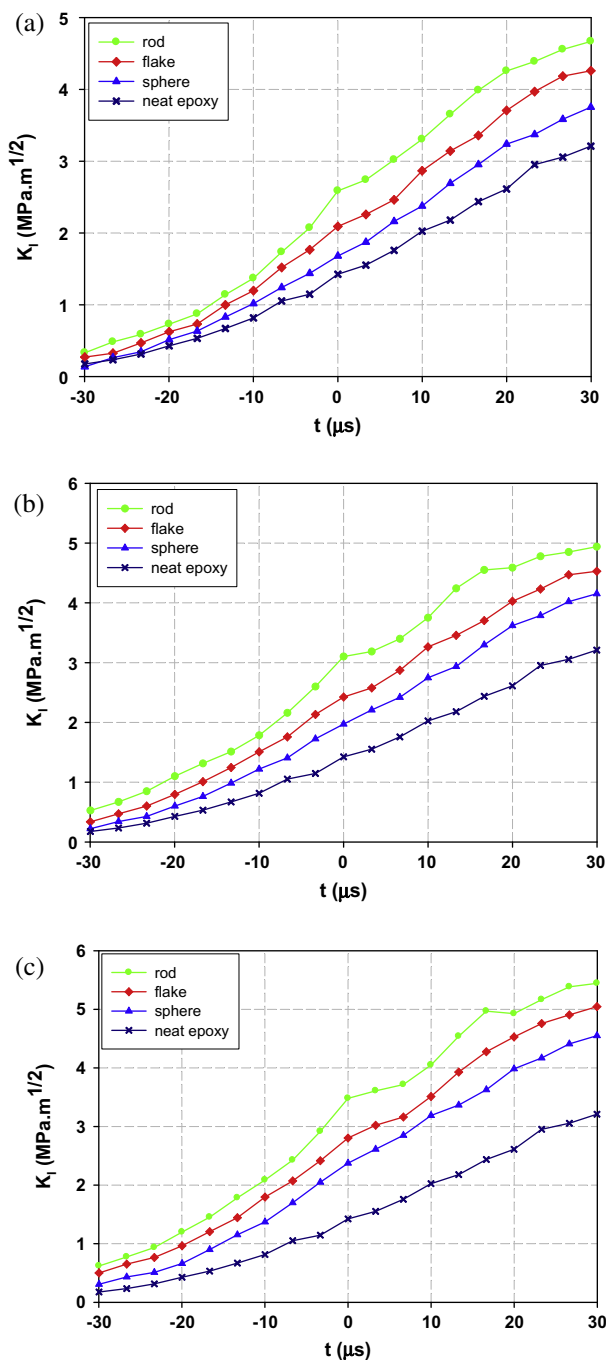

Fig. 5. Experimental repeatability of SIF histories for 15% rod-shaped glass-filled epoxy for the 'Al-PS' case and comparison with FE simulation. (Histories for K_{II} are also provided for completeness. Being a symmetric loading experiment, K_{II} histories are relatively small but useful to estimate errors in the least-squares analysis scheme).

Fig. 6. Finite element mesh used for elasto-dynamic simulation of mode-I fracture experiments using ABAQUS/explicit (left); strain history recorded on the long-bar for the 'Al-PS' case (right).

Table 3
Crack initiation toughness (in MPa√m) comparison for different filler shapes at different V_f using an aluminum pulse shaper ('Al-PS') during impact (% improvement is relative to neat epoxy).

Volume fraction		Crack initiation toughness		
0% (Neat epoxy)		1.42 ± 0.06		
		Sphere	Flakes	Rods
5%		1.68 ± 0.07	2.09 ± 0.09	2.59 ± 0.11
	Improvement in K_I	18%	47%	82%
10%		1.97 ± 0.14	2.43 ± 0.11	3.10 ± 0.16
	Improvement in K_I	39%	71%	118%
15%		2.38 ± 0.13	2.80 ± 0.16	3.48 ± 0.16
	Improvement in K_I	68%	97%	145%

Fig. 7. K_I histories (a) for 5% V_f, (b) 10% V_f, (c) 15% V_f glass-filled epoxy for the Aluminum 1100 pulse shaper ('Al-PS') case with different filler particle shape.

Fig. 8. Fractographs of 10% V_f sphere, flake, rod-shaped glass-filled epoxy (top to bottom respectively) for the 'Al-PS' pulse shaper case; scale bar = 100 μm.

flake and spherical filler cases showed 82%, 47% and 18% improvement, respectively, in crack initiation toughness relative to that for neat epoxy. The 10% V_f (Fig. 7(b)) rod, flake and spherical filler cases showed 118%, 71% and 39% improvement, respectively, in crack initiation toughness compared to neat epoxy. Furthermore, as expected, for 10% V_f, the SIF histories of each type of filler showed a higher value when compared to the 5% V_f composites. For 15% V_f (Fig. 7(c)) rod, flake and spherical filler cases showed 145%, 97% and 68% improvement, respectively, in crack initiation toughness compared to neat epoxy. Again, as expected, 15% V_f SIF histories of each type of the filler showed a higher value when compared to both 5% and 10% V_f counterparts.

A fractographic study was carried out to understand the underlying toughening mechanisms for the dramatic improvement in fracture responses due to filler shape change. It should be first noted that fracture surface micrographs (Fig. 8) show no agglomeration of filler particles in all cases and filler distribution is uniform. As the stress waves propagate through the specimen, the crack front is driven forward until it encounters filler particles. A careful observation of fractographs suggests that interaction of the crack front with filler phase leads to the following potential failure modes: (a) matrix cracking, (b) filler–matrix interface separation, (c) filler pullout, (d) filler breakage. During crack growth each active failure mode contributes to energy dissipation which adds to the overall increase in fracture toughness of the composite. In case of spherical fillers, matrix cracking and inclusion-matrix debonding were found to be the dominant modes. A few spherical fillers were pulled out but none of them were found fractured. Therefore due to a low aspect ratio (= 1 in this case), crack bridging can be assumed inactive (or minimum) and the crack circumvented the inclusion by crack deflection and/or debonding of the interface causing momentary crack front arrest and reinitiation. In case of flakes, fracture surface is dominated by matrix cracking, inclusion-matrix debonding and filler breakage. The breakage of flakes contributes to extra energy dissipation besides crack deflection and trapping mechanisms. All these contribute to an increase in fracture toughness when compared to spherical filler counterpart. For rod-shaped filler, the failure modes were matrix cracking, inclusion-matrix debonding and filler breakage with evidence of filler pullout. On the fracture surface, several broken short fibers were identified. Since the average fiber length was ∼800 μm, it is likely fiber bridges across the crack front resisted crack growth, before eventually getting pulled out of the matrix or fractured as the crack grew. The tensile strength of the fibers being ∼3 GPa (compared to that of neat epoxy of ∼70 MPa), even a few fiber breakages could result in a rather high apparent fracture toughness of the composite.

The fracture surface features such as roughness and tortuosity scale with energy dissipation during crack propagation [30]. Hence,
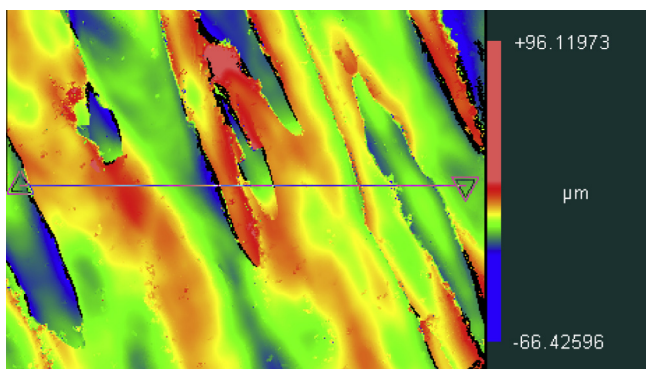

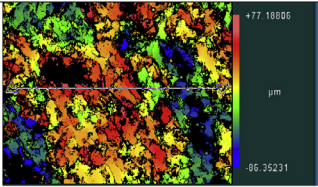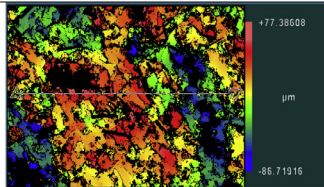**Fig. 9.** Typical fracture surface profile of neat epoxy for the 'Al-PS' pulse shaper case (R_a = 6.3 μm).
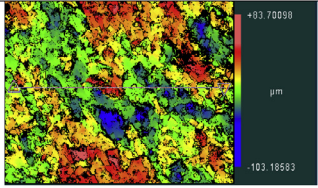
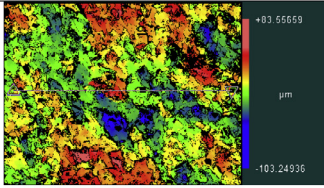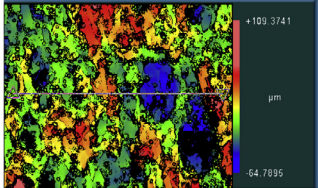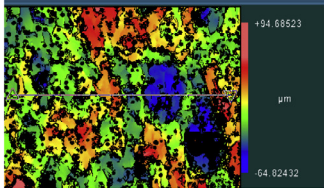|	Before Masking	After Masking	K_I (MPa√m)
Rods	R_a = 24.9 μm	R_a = 24.8 μm	3.10
Flakes	R_a = 15.5 μm	R_a = 15.4 μm	2.43
Spheres	R_a = 19.2 μm	R_a = 19.1 μm	1.97

Fig. 10. Typical pseudo-colored fracture surfaces of glass-filled epoxy (10% V_f) for the 'Al-PS' pulse shaper case. Fillers contribute less than ∼1% to the overall surface roughness (R_a).

fracture surfaces were profiled using white light interferometry (Zygo New View 6000) at a magnifications of 10× (20× Mirau lens with a 0.5× Zoom). Nine fields of view were stitched together to obtain a total sample surface of 1.91 × 1.43 mm, with an areal resolution of 1 μm and vertical resolution better than 10 nm. To determine the effect of filler particles on surface roughness measurements, surfaces were analyzed for surface roughness both before and after employing a masking procedure to remove regions containing filler particles in the images.

Fig. 9 shows a typical false-color image of the fracture surface of neat epoxy. It appears relatively smooth with a measured roughness (R_a) of 6.3 μm. Fig. 10 shows typical fracture surfaces of samples with different fillers at 10% V_f. All samples have a higher surface roughness than neat epoxy, ranging from R_a = 15.5 μm for flakes, to R_a = 24.9 μm for rods. To test the effect of the filler on the overall surface roughness, masks were created in the Zygo Metro-Pro analysis software. Each mask was developed to remove data points/regions representing the fillers. Typical data sets showing before and after the masking operation are shown in Fig. 10. The filler materials have very little effect on the overall surface roughness, in all cases contributing <1% to the R_a value. Thus, while fillers might contribute to the overall roughness at smaller scales, the roughness at larger scales is primarily due to crack propagation behavior.

The surface roughness measurements indicate higher R_a for spherical fillers than flakes although macromeasurements show higher stress intensity factors for the sample with flakes. The fractographic evaluation explains this apparent inconsistency for this. During crack growth, each failure mechanism contributes to energy dissipation which adds to the overall increase in fracture toughness of the PPC. In case of spheres, only filler pull out and filler-matrix interface separations besides matrix cracking were found. None of the spheres were found broken whereas in case of flakes an extra failure mode namely filler breakage was found. This additional failure mode provides more energy absorption due to higher tensile strength of glass flakes.

7.2. Effect of filler volume fraction

For each filler shape, dynamic K_I histories were compared for 0%, 5%, 10% and 15% filler V_f, respectively, when an aluminum pulse shaper ('Al-PS') was used. In each case, K_I showed an increasing trend with volume fraction of the filler during the entire fracture event. The rate of increase of K_I followed the above volume fractions trend up to crack initiation. The rate of increase of K_I was approximately constant for all volume fractions, once the crack started propagation. For spherical-fillers (Fig. 11(a)), 5%, 10% and 15% V_f showed 18%, 39% and 68% improvement, respectively, in crack initiation toughness compared to neat epoxy. For flakes (Fig. 11(b)), 5%, 10% and 15% V_f the improvements were 47%, 71% and 97%, respectively, relative to neat epoxy. For rods (Fig. 11(c)), on the other hand, showed 82%, 118% and 145% improvement, respectively, for 5%, 10% and 15% filler V_f compared to neat epoxy. It should also be noted that a noticeable slope change in K_I histories are evident when the crack initiates at 15% filler V_f. A summary of crack initiation toughness values and the corresponding enhancements for all the different cases are provided in Table 3.

7.3. Quantification of shape effects on crack initiation toughness

To obtain the functional form of dependence of dynamic crack initiation toughness on the filler aspect ratio, the measured values were plotted as a function of the log of aspect ratio (AR) (see, Table 1) for each filler shape at 5%, 10% and 15% V_f (Fig. 12) for the 'Al-PS' case. For all the three volume fractions, K_I vs log(AR) plots were essentially linear. Further, crack initiation toughness

increases with aspect ratio and follows a linear relationship of the form $K_I = C_1 * \log(AR) + C_2$, where C_1 and C_2 are constants (for 5% V_f: C_1 = 0.49 MPa$\sqrt{}$m and C_2 = 1.69 MPa$\sqrt{}$m, for 10% V_f: C_1 = 0.59 MPa$\sqrt{}$m and C_2 = 1.97 MPa$\sqrt{}$m and for 15% V_f: C_1 = 0.58 MPa$\sqrt{}$m and C_2 = 2.37 MPa$\sqrt{}$m). For all the three V_f considered here, C_1 is nearly independent of V_f. Fractography previously revealed that interaction between the crack front and the rod-shaped filler with maximum aspect ratio contributed to various crack bridging mechanism during crack propagation which in turn contributed to energy dissipation during crack growth. This resulted in higher fracture toughness whereas in case of flakes
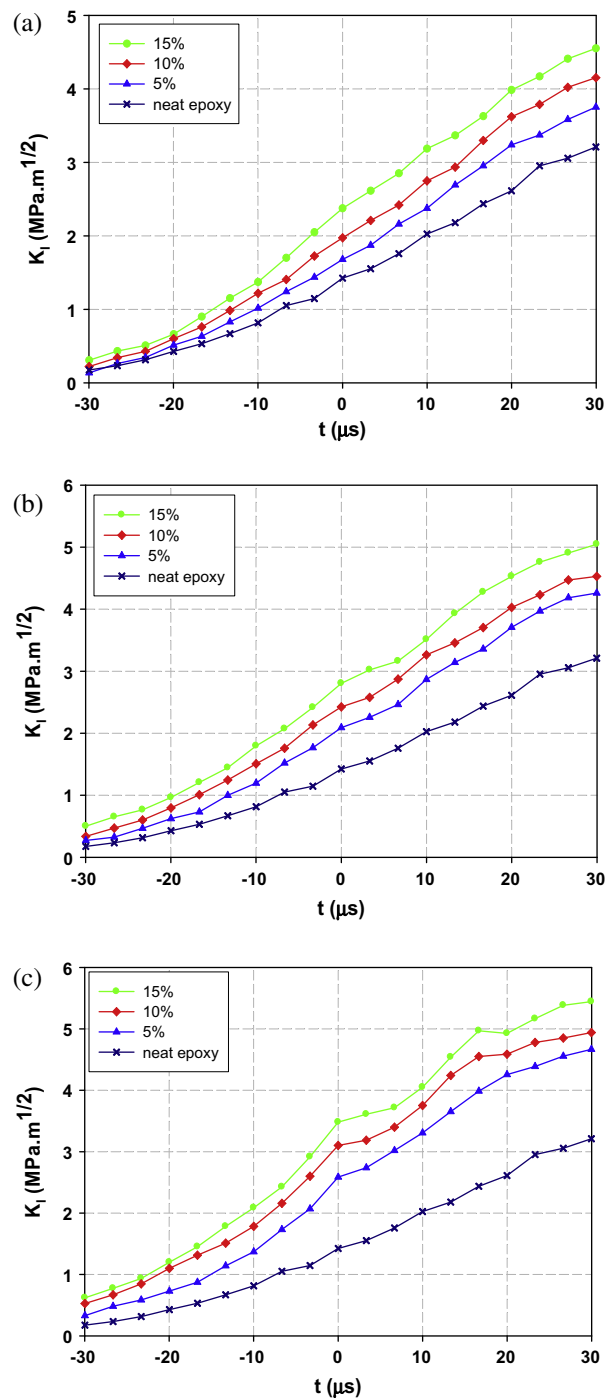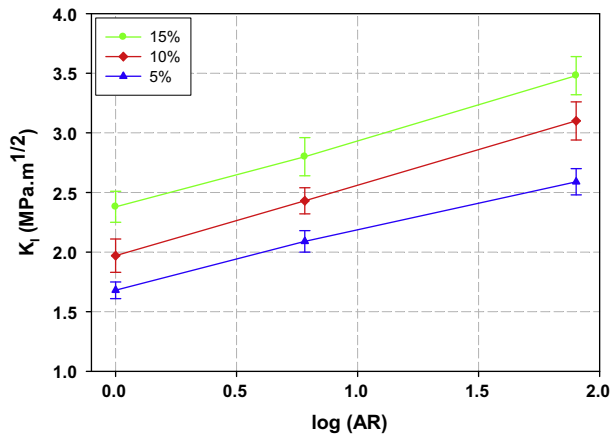

Fig. 11. K_I histories for glass-filled epoxy with (a) spherical filler, (b) flakes, (c) rods for the 'Al-PS' pulse shaper case with different volume fractions.

Fig. 12. Effect of aspect ratio on crack initiation toughness for the 'Al-PS' pulse shaper case. Error bars indicate one standard deviation relative to the average toughness value. The crack initiation toughness follows a linear relationship of the form $K_I = C_1 * \log(AR) + C_2$, where C_1 and C_2 are constants (for 5% V_f: $C_1 = 0.49$ MPa$\sqrt{m}$ and $C_2 = 1.69$ MPa$\sqrt{m}$; for 10% V_f: $C_1 = 0.59$ MPa$\sqrt{m}$ and $C_2 = 1.97$ MPa$\sqrt{m}$ and for 15% V_f: $C_1 = 0.58$ MPa$\sqrt{m}$ and $C_2 = 2.37$ MPa$\sqrt{m}$.).

and sphere due to their relatively lower aspect ratio crack front generally avoided the filler typically by circumventing it.

7.4. Effect of loading rate

Previous sections show that filled-epoxy with rod-shaped fillers produce the highest enhancement in crack initiation and post-initiation toughness among the three different fillers shapes considered. Accordingly, the loading rate effects were examined for this particular case using composites containing 10% V_f of the

Table 4
Crack initiation toughness (in MPa$\sqrt{m}$) comparison (% improvement is relative to the neat epoxy of the respective pulse shaper used during loading).

| Pulse shaper type	Crack initiation toughness	Neat epoxy	Rods (10% V_f)
'Quasi-static'	K_I	1.92 [5]	2.48 ± 0.02
	Improvement in K_I	–	29%
'PC-PS'	K_I	1.22 ± 0.07	2.60 ± 0.08
	Improvement in K_I	–	113%
'Al-PS'	K_I	1.42 ± 0.05	3.10 ± 0.16
	Improvement in K_I	–	118%
'No-PS'	K_I	2.28 ± 0.15	3.42 ± 0.17
	Improvement in K_I	–	50%
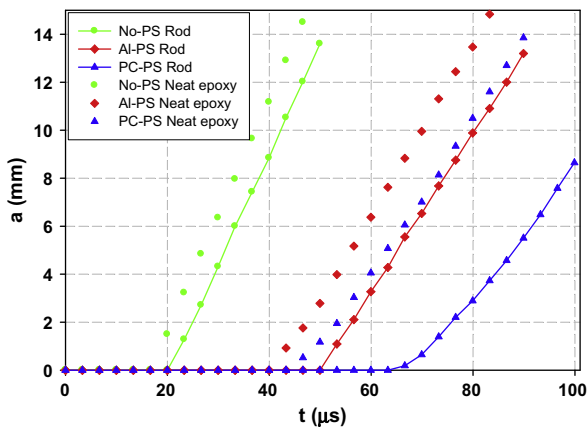
Fig. 13. Crack growth history plots for neat epoxy and 10%V_f rod-filled epoxy at different loading rates.

filler. The rate effects were studied by comparing the crack growth histories and stress intensity factor produced by the three different pulse shapers (Table 4). The crack length histories are plotted for both the neat epoxy and the 10% V_f glass-filled epoxy in Fig. 13. Crack initiation time instants and crack speeds are tabulated in Table 5. Time $t = 0$ is the time instant when the long-bar impacts the specimen. Due to the reinforcement, PPCs with rod-shaped filler resisted crack initiation for a longer duration when compared to the neat epoxy counterpart studied using the same pulse shaper. The crack propagation was also faster in neat epoxy compared to filled epoxy for each pulse shaper case. Plots of K_I histories are shown in Fig. 14(a) and (b) for the neat epoxy and the 10% V_f filled-epoxies, respectively. The K_I histories show a monotonic increase until and after crack initiation for all the three pulse shapers for both the filled and neat epoxy cases. In each case, the

Table 5
Crack initiation time and crack speed comparison for neat epoxy and 10% V_f rod-filled epoxy.

Pulse shaper type	Crack initiation time (μs)		Crack speed (m/s)	
	Neat epoxy	Rods (10% V_f)	Neat epoxy	Rods (10% V_f)
'No-PS'	17	20	486 ± 29	462 ± 35
'Al-PS'	40	50	358 ± 11	332 ± 26
'PC-PS'	43	63	306 ± 14	256 ± 13
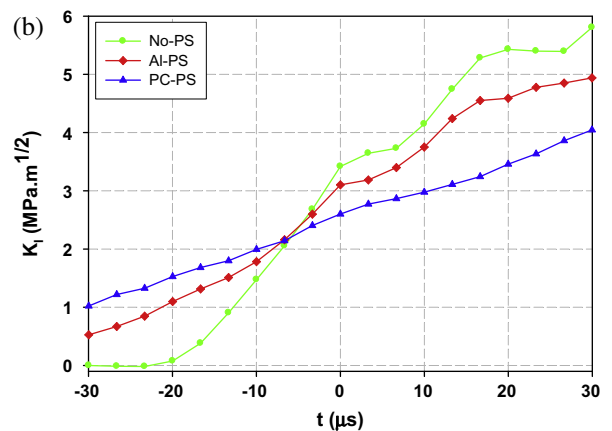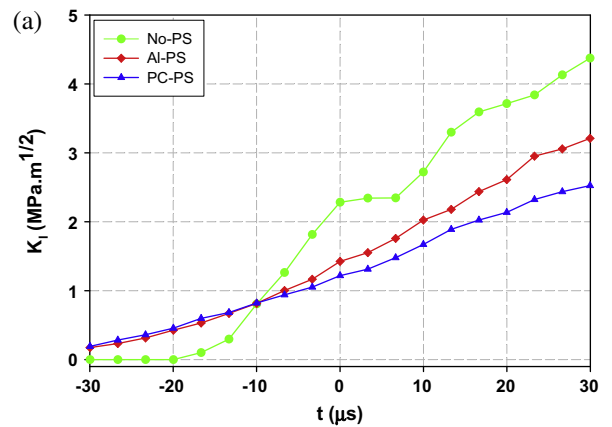
Fig. 14. SIF histories at different loading rates: (a) For neat epoxy (Before crack initiation, dK_I/dt were $\sim 149 \times 10^3$, 61×10^3 and 40×10^3 MPa$\sqrt{m}$/s for 'No-PS', 'Al-PS' and 'PC-PS' cases, respectively, compared to dK_I/dt of $\sim 6 \times 10^{-2}$ MPa$\sqrt{m}$/s in quasi-static loading case.), (b) for glass-filled epoxy (10% V_f) (Before crack initiation, dK_I/dt were $\sim 182 \times 10^3$, 132×10^3 and 53×10^3 MPa$\sqrt{m}$/s for 'No-PS', 'Al-PS' and 'PC-PS' cases, respectively, compared to dK_I/dt of $\sim 1 \times 10^{-1}$ MPa$\sqrt{m}$/s in quasi-static loading case (Appendix A).).
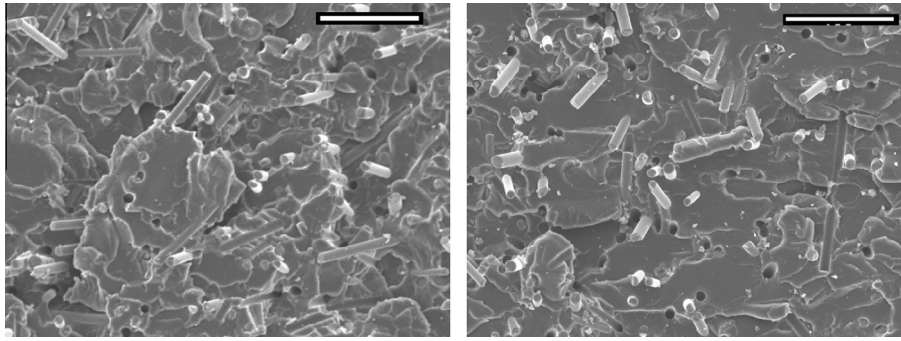
Fig. 15. Fractographs of glass-filled epoxy (10% V_f) for the highest ('No-PS' case (left)) and the lowest ('PC-PS' case (right)), respectively; scale bar = 100 μm.

loading rate was characterized by dK_I/dt [31] by measuring the slope of the K_I history in the linearly increasing region up to crack initiation. For neat epoxy, before crack initiation, K_I histories show higher slope for the 'No-PS' ($dK_I/dt = 149 ± 12 × 10^3$ MPa$\sqrt{}$m/s) case followed by the 'Al-PS' ($dK_I/dt = 61 ± 8 × 10^3$ MPa$\sqrt{}$m/s) and 'PC-PS' ($dK_I/dt = 40 ± 7 × 10^3$ MPa$\sqrt{}$m/s) cases, respectively and for 10% filled-epoxy, K_I histories show slightly higher slopes for the 'No-PS' ($dK_I/dt = 182 ± 11 × 10^3$ MPa$\sqrt{}$m/s) case followed by the 'Al-PS' ($dK_I/dt = 132 ± 16 × 10^3$ MPa$\sqrt{}$m/s) and 'PC-PS' ($dK_I/dt = 53 ± 4 × 10^3$ MPa$\sqrt{}$m/s) cases, respectively. For neat epoxy, K_I history showed a drop at crack initiation for the 'No-PS' case corresponding to the highest loading rate. For 10% filled epoxy in 'No-PS' and 'Al-PS' cases, a small kink in the histories are noticeable. The 'No-PS' case produces the highest crack initiation toughness as well as post-initiation K_I values and 'Al-PS' and 'PC-PS' cases, respectively, follow for both the neat epoxy and filled-epoxy. For neat epoxy, the rate of increase of K_I was approximately constant for the 'Al-PS' and 'PC-PS' cases but lower than the 'No-PS' case, whereas for filled-epoxy, the rate of increase of K_I was approximately constant for the 'No-PS' and 'Al-PS' cases but greater than the 'PC-PS' case, once the crack initiated. The filled epoxies show 113%, 118% and 50% increase in crack initiation toughness for the 'PC-PS', 'Al-PS' and 'No-PS' cases, respectively, compared to the neat epoxy studied using the respective pulse shaper. This comparison, though not strictly rigorous due to different dK_I/dt between filled and neat samples, it provides a good estimation of loading rate effects.

The fractographic study was carried out on filled epoxy for different pulse shaper cases to understand the underlying toughening mechanisms on crack initiation toughness due to loading rate differences. In Fig. 15, micrographs of 10% V_f glass-filled epoxy with rod-shaped filler for the 'No-PS' case (left) and the 'PC-PS' case (right) are shown, respectively. It is evident that the surface ruggedness is noticeably higher for the 'No-PS' case compared to the 'PC-PS' case. Also, for higher loading rate, filler-matrix interface separation mode is substantially higher for the 'No-PS' case than the 'PC-PS' case. The fibers bridging the crack faces result in an overall stiffer response at the higher loading rate and they likely break before being pulled out of the matrix during crack growth. The reported tensile strength of the fibers being ∼3 GPa, the process contributes to a rather high apparent crack initiation and propagation SIF values for the PPC. More fiber pullouts were found in the 'PC-PS' case than the 'No-PS' case, explaining the lowest crack initiation toughness in the 'PC-PS' case among all the three pulse shapers. However for neat epoxy, the only failure mode was matrix cracking. At higher loading rate neat epoxy resisted crack growth via microscopic crack branches producing higher surface roughness (not shown for brevity).

8. Conclusion

In the present study, the effects of filler shape (characterized by the aspect ratio), filler volume fraction and loading rate on fracture toughness were investigated. Digital Image Correlation method was used in conjunction with high-speed photography for studying dynamic fracture histories. The experiments were carried out on pre-notched glass-filled epoxy specimens using a setup comprised of a long-bar impactor aided by a gas-gun delivering one-point impact to an unconstrained specimen. The following major conclusions were drawn from this study.

- For all three filler shapes – flakes, rods and spheres, crack initiation toughness increased significantly with filler volume fraction.
- For epoxy filled with spherical filler, 5%, 10% and 15% V_f cases showed 18%, 39% and 68% improvement, respectively; for those reinforced with flakes, 5%, 10% and 15% V_f cases showed 47%, 71% and 97% improvement, respectively and for epoxy filled with rod-shaped fillers; at 5%, 10% and 15% V_f showed 82%, 118% and 145% improvement, respectively, in terms of crack initiation fracture toughness when compared to neat epoxy.
- For all three different volume fractions considered, the rod-shaped fillers produce the highest crack initiation toughness as well as post-initiation SIF values followed by flakes and spheres, respectively.
- At 5% V_f, filled epoxy with rods, flakes and spheres showed 82%, 47% and 18% improvement, respectively, at 10% V_f, filled epoxy with rods, flakes and spheres showed 118%, 71% and 39% improvement, respectively, and at 15% V_f, filled epoxy with rods, flakes and spheres showed 145%, 97% and 68% improvement, respectively, in crack initiation fracture toughness compared to neat epoxy.
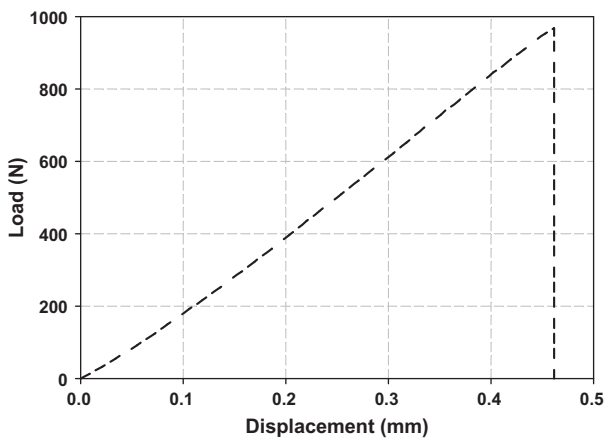

Fig. A1. Load–displacement response of 10% V_f rod-filled epoxy in quasi-static fracture test.

- The fractographic evaluation explained the different mechanisms associated with different filler shapes during dynamic fracture and their contribution in enhancing fracture toughness. Among all existing failure modes, filler breakage is most preferred due to its higher strength compared to neat epoxy. Even a few filler breakages could contribute significantly to a rather high apparent fracture toughness of the PPC.
- Three different loading rates were achieved through the usage of different pulse shapes between the striker and the long-bar. As the loading rate increased, PPC showed a stiffer response and produced higher crack initiation toughness.
- The crack initiated earlier in neat epoxy compared to 10% V_f filled epoxy with rod-shaped filler for all the loading rates used. Also, the crack speed was higher in neat epoxy compared to 10% V_f filled epoxy with rod-shaped filler for all the three loading cases used.
- At 10% V_f filled epoxy with rod-shaped filler showed 113%, 118% and 50% increase in crack initiation toughness for the 'PC-PS', 'Al-PS' and 'No-PS' cases, respectively, compared to the neat epoxy of the respective pulse shaper case.

Acknowledgements

Appendix A

A.1. Quasi-static fracture tests

For completeness, quasi-static crack initiation toughness measurements were also performed for the 10% V_f rod-shaped glass-filled epoxy. The glass-filled sheets with rod-shaped fillers were cast and machined into rectangular specimens having dimensions of 90 mm × 30 mm × 9 mm. An edge notch of 6 mm length was introduced at the mid-span of each specimen using diamond impregnated circular saw and the notch tip sharpened using a sharp razor blade. Fracture tests were carried out in symmetric three-point bending configuration in displacement control mode with a cross-head speed of 1.27 mm/min using Instron 4465. The load–displacement response was linear up to crack initiation following by an abrupt fracture in the specimen (Fig. A1). The quasi-static fracture toughness was calculated using

$$K_{IC} = \frac{\left(\frac{P_{max}}{B\sqrt{W}}\right)\left(3\frac{S}{W}\sqrt{\frac{a}{W}}\right)}{2\left(1+2\frac{a}{W}\right)\left(1-\frac{a}{W}\right)^{1.5}}\left[1.99 - \frac{a}{W}\left(1-\frac{a}{W}\right)\left\{2.15 - 3.93\left(\frac{a}{W}\right)\right.\right.$$
$$\left.\left. + 2.7\left(\frac{a}{W}\right)^2\right\}\right]$$

where P_{max} is the maximum load prior to fracture, a is crack length, B is thickness, W is width and, S is span. The crack initiation toughness K_{IC} for the neat epoxy and 10% V_f rod-shaped glass-filled epoxy were 1.92 [5] MPa$\sqrt{}$m and 2.48 ± 0.08 MPa$\sqrt{}$m, respectively.

References

[1] Fu SY, Feng XQ, Lauke B, Mai YW. Effects of particle size, particle/matrix interface adhesion and particle loading on mechanical properties of particulate-polymer composites. Compos B Eng 2008;39(6):933–61.

[2] Koh SW, Kim JK, Mai YW. Fracture-toughness and failure mechanisms in silica-filled epoxy-resin composites – effects of temperature and loading rate. Polymer 1993;34(16):3446–55.

[3] Kargerkocsis J, Friedrich K. Temperature and strain-rate effects on the fracture-toughness of poly(ether ether ketone) and its short glass-fiber reinforced composite. Polymer 1986;27(11):1753–60.

[4] Nakamura Y, Okabe S, Iida T. Effects of particle shape, size and interfacial adhesion on the fracture strength of silica-filled epoxy resin. Polym Polym Compos 1999;7(3):177–86.

[5] Jajam KC, Tippur HV. Quasi-static and dynamic fracture behavior of particulate polymer composites: a study of nano- vs. micro-size filler and loading-rate effects. Compos B Eng 2012;43(8):3467–81.

[6] Liu HY, Wang GT, Mai YW, Zeng Y. On fracture toughness of nano-particle modified epoxy. Compos B Eng 2011;42(8):2170–5.

[7] Liang JZ. Reinforcement and quantitative description of inorganic particulate-filled polymer composites. Compos B Eng 2013;51:224–32.

[8] Park BG, Crosky AG, Hellier AK. Fracture toughness of microsphere Al$_2$O$_3$–Al particulate metal matrix composites. Compos B Eng 2008;39(7–8):1270–9.

[9] Kushvaha V, Tippur H. Effect of filler particle shape on dynamic fracture behavior of glass-filled epoxy. In: Conference proceedings of the society for experimental mechanics series; 2012. 1(Dynamic Behavior of Materials): p. 513–22.

[10] Song SG, Shi N, Gray GT, Roberts JA. Reinforcement shape effects on the fracture behavior and ductility of particulate-reinforced 6061-Al matrix composites. Metall Mater Trans A – Phys Metall Mater Sci 1996;27(11):3739–46.

[11] Nakamura Y, Yamaguchi M, Okubo M, Matsumoto T. Effect of particle-size on the fracture toughness of epoxy-resin filled with spherical silica. Polymer 1992;33(16):3415–26.

[12] Wu TT. The effect of inclusion shape on the elastic moduli of a two-phase material. Int J Solids Struct 1966;2:1–8.

[13] Spanoudakis J, Young RJ. Crack-propagation in a glass particle-filled epoxy-resin. 1. Effect of particle-volume fraction and size. J Mater Sci 1984;19(2):473–86.

[14] Nakamura Y, Yamaguchi M, Kitayama A, Okubo M, Matsumoto T. Effect of particle-size on mechanical properties of epoxy-resin filled with angular-shaped silica. J Appl Polym Sci 1992;44(1):151–8.

[15] Kitey R, Tippur HV. Role of particle size and filler-matrix adhesion on dynamic fracture of glass-filled epoxy. I. Macromeasurements. Acta Mater 2005;53(4):1153–65.

[16] Jacob GC, Starbuck JM, Fellers JF, Simunovic S, Boeman RG. Fracture toughness in random-chopped fiber-reinforced composites and their strain rate dependence. J Appl Polym Sci 2006;100(1):695–701.

[17] Compston P, Jar PYB, Davies P. Matrix effect on the static and dynamic interlaminar fracture toughness of glass–fibre marine composites. Compos B Eng 1998;29(4):505–16.

[18] Compston P, Jar PYB, Burchill PJ, Takahashi K. The effect of matrix toughness and loading rate on the mode-II interlaminar fracture toughness of glass-fibre/vinyl-ester composites. Compos Sci Technol 2001;61(2):321–33.

[19] Kusaka T, Hojo M, Mai YW, Kurokawa T, Nojima T, Ochiai S. Rate dependence of mode I fracture behaviour in carbon-fibre/epoxy composite laminates. Compos Sci Technol 1998;58(3–4):591–602.

[20] Lee D, Tippur HV, Bogert P. Quasi-static and dynamic fracture of graphite/epoxy composites: an optical study of loading-rate effects. Compos B Eng 2010;41(6):462–74.

[21] Kushvaha V, Branch A, Tippur H. Effect of loading rate on dynamic fracture behavior of glass and carbon fiber modified epoxy. Dyn Behav Mater 2014;1:169–76.

[22] Kitey R, Tippur HV. Dynamic crack growth past a stiff inclusion: optical investigation of inclusion eccentricity and inclusion-matrix adhesion strength. Exp Mech 2008;48(1):37–53.

[23] Bedsole R, Tippur HV. Dynamic fracture characterization of small specimens: a study of loading rate effects on acrylic and acrylic bone cement. J Eng Mater Technol 2013;135(3):031001–11.

[24] Frew DJ, Forrestal MJ, Chen W. A split hopkinson pressure bar technique to determine compressive stress-strain data for rock materials. Exp Mech 2001;41(1):40–6.

[25] James W, Dally WFR. Experimental stress analysis. McGraw-Hill; 1991.

[26] Nishioka T, Atluri SN. Path-independent integrals, energy-release rates, and general-solutions of near-tip fields in mixed-mode dynamic fracture-mechanics. Eng Fract Mech 1983;18(1):1–22.

[27] Tippur HV, Krishnaswamy S, Rosakis AJ. Optical mapping of crack-tip deformations using the methods of transmission and reflection coherent gradient sensing – a study of crack-tip K-dominance. Int J Fract 1991;52(2):91–117.

[28] Kaiser, M.A., Advancements in the Split Hopkinson Bar Test; Page:27 (Equation 3.27), in Mechanical Engineering. 1998, Virginia Polytechnic Institute and State University: Blacksburg, Virginia.

[29] Kirugulige MS, Tippur HV, Denney TS. Measurement of transient deformations using digital image correlation method and high-speed photography: application to dynamic fracture. Appl Opt 2007;46(22):5083–96.

[30] Sharon E, Gross SP, Fineberg J. Energy dissipation in dynamic fracture. Phys Rev Lett 1996;76(12):2117–20.

[31] Janssen M, Zuidema J, Wanhill R. Fracture mechanics. 2nd ed. CRC Press; 2004. Page no. 176.